Fatigue crack propagation behaviour in wire+arc additive manufactured Ti-6Al-4V: Effects of microstructure and residual stress

Zhang, J, Wang, X, Paddea, S & Zhang, X

Original citation & hyperlink:
Zhang, J, Wang, X, Paddea, S & Zhang, X 2016, 'Fatigue crack propagation behaviour in wire+arc additive manufactured Ti-6Al-4V: Effects of microstructure and residual stress' Materials and Design, vol 90, pp. 551-561. DOI: 10.1016/j.matdes.2015.10.141
https://dx.doi.org/10.1016/j.matdes.2015.10.141

DOI 10.1016/j.matdes.2015.10.141
ISSN 0261-3069
ESSN 0264-1275

Publisher: Elsevier

Published in: Materials and Design 90 (2016) 551–561 | http://dx.doi.org/10.1016/j.matdes.2015.10.141

Fatigue Crack Propagation Behaviour in Wire+Arc Additive Manufactured Ti-6Al-4V: Effects of Microstructure and Residual Stress

Jikui Zhang[a], Xueyuan Wang[b, c], Sanjooram Paddea[d], Xiang Zhang[*b, c]

[a] Department of Aircraft Design, Beihang University, Beijing, 100191, P.R. China
[b] School of Engineering, Cranfield University, Bedford MK43 0AL, UK
[c] Now at: Faculty of Engineering and Computing, Coventry University, Coventry CV1 5FB, UK
[d] The Open University, Walton Hall, Milton Keynes MK7 6AA, UK

Abstract

Fatigue crack propagation tests of Ti-6Al-4V fabricated by the Wire+Arc Additive Manufacturing (WAAM) process are analysed. Crack growth rate and trajectory are examined before and after the crack tip crossing an interface between the WAAM and wrought alloys. The study has focused on the microstructure and residual stress effect. First, the differences in crack growth rate and path between WAAM and wrought alloys are attributed to their different microstructure; the equiaxed wrought alloy has straight crack path, whereas the WAAM lamellar structure causes tortuous crack path resulting in lower crack growth rate. Second, based on measured residual stress profile in the as-built WAAM piece, retained residual stress in the much smaller compact tension specimens and its effect on crack growth rate are calculated by the finite element method. Numerical simulation shows considerable residual stress in the test specimen and the stress magnitude depends on the initial crack location and propagation direction in relation to the WAAM-wrought interface. Residual stress is released immediately if the initial crack is in the wrought substrate; hence it has little effect. In contrast, when crack grows from WAAM to wrought, residual stress is retained resulting in higher stress intensity factor; hence greater crack growth rate.

Keywords: Additive manufacturing, titanium alloy, fatigue crack propagation, residual stress, microstructure

1. Introduction

Titanium alloys are widely used in the airframes and safety critical systems owing to their excellent mechanical properties, including high specific strength, outstanding resistance to fatigue, high temperature and corrosion, and compatibility with carbon fiber composite materials that are increasingly used in the airframes. However, manufacturing of titanium components by conventional machining processes is difficult and costly due to several inherent properties, such as the low thermal conductivity and high chemical reactivity with many cutting tool materials, which can lead to premature failure of the machining tools and reduced productivity [1,2]. In recent years the additive manufacturing (AM) technologies have been rapidly developed owing to their capability of near-net shape fabrication of complex shapes without dies or substantial machining, resulting in reductions in the lead-time, material waste and cost [3,4].

The Wire+Arc Additive Manufacturing (WAAM) [5,6], which feeds a wire at a controlled rate into an electric or plasma arc to melt the wire onto a substrate or previously deposited layer, is a developing AM technology that has found applications in the aerospace and other industrial sectors. Comparing with the powder based AM processes by laser or electron beam, WAAM has much higher material deposition rate, lower cost and no requirement for powder handling. However, the raw WAAM parts have lower accuracy in dimension and surface roughness resulting in significant amount of post-process machining [7]. The benefit

* Corresponding author's current address: Coventry University, T: +44 24 77658599; E: xiang.zhang@coventry.ac.uk (X Zhang)
Co-authors: zjk@buaa.edu.cn (J. Zhang); wangx75@uni.coventry.ac.uk (X. Wang); Sanjooram.paddea@open.ac.uk (S. Paddea)

of reducing material waste and machining cost is significant for high strength titanium alloys that are very expensive and hard to machine comparing with other aerospace alloys. One of the challenges to widespread use of additive manufacturing to build safety critical structural parts has been recognised as the qualification and certification of the in-service performance [4]. Therefore it is necessary to assess the mechanical properties of titanium alloys built by WAAM. Changes in the microstructure and process induced residual stress are the main factors affecting the mechanical properties of WAAM deposited components [8].

Ti-6Al-4V is a typical α+β titanium alloy that is widely used in the aerospace industry due to the good balance of strength, ductility, fatigue and fracture properties. The microstructure of Ti-6Al-4V can be modified by using appropriate heat treatment either above the β transus temperature or in the α-β field [9] and it plays an important role in improving the mechanical properties. Previous studies [5, 6, 10-11] have shown that the β grain of WAAM Ti-6Al-4V is similar to those AM alloys deposited by laser [12,13] or electron beam [14]. The macrostructure of WAAM Ti-6Al-4V is characterized by the epitaxial growth of coarse columnar prior-β grains upwards through the deposited layers, Furthermore, the microstructure of WAAM Ti-6Al-4V consists of fine Widmanstätten α in the upper deposited layers and a banded coarsened Widmanstätten lamellar α in the lower layers [15]. This difference in microstructure is owing to the repeated rapid heating and cooling thermal cycles during the WAAM process. The coarse lamellar microstructure is also observed in other AM built titanium alloys [4,16,17], which is proved to be beneficial to the resistance to fatigue crack growth [9,18]. Comparing with a forged bar, the average yield and ultimate tensile strengths of WAAM Ti-6Al-4V are slightly lower, ductility is similar and mean fatigue life is considerably longer [15,19]. Furthermore, the as-deposited WAAM Ti-6Al-4V exhibited direction dependent mechanical properties. The average yield and ultimate tensile strengths are higher in the longitudinal direction than that in the transverse direction [15]. Fracture toughness is similar to that of typical wrought Ti-6Al-4V, and is greater in the longitudinal direction than the transverse direction [20]. Fatigue crack growth rate is slightly greater in the longitudinal than the transverse direction [21]. In the literature, the welding torch movement direction is defined as the longitudinal direction (L) and the layer build direction is the transverse (T), as shown in Fig.1. For the selective laser melted [22] and electron beam melted Ti-6Al-4V [23], no noticeable difference was observed in the crack growth rate in the Paris law region (Region II) between the longitudinal and transverse directions. Both the WAAM [21] and electron beam melted [23] Ti-6Al-4V exhibit lower crack growth rate in both the longitudinal and transverse directions than that in the wrought alloy (isotropic) in the Region II.

Residual stress exists in AM parts due to the thermal contraction of the material in the melting and rapid cooling process [24]. Residual stress can be either beneficial or detrimental depending on its sign, magnitude and distribution with respect to the crack orientation and local stress. Attempts have been made to quantify residual stress in AM parts [24-26]. For example, Rangaswamy et al. [25] used the neutron diffraction method to measure parts produced by the LENS process (a powder based AM) and found significant compressive residual stress in the parts, which results in increased fatigue life owing to the crack closure effect that reduces the crack growth rate [27]. Paradowska et al. showed that the peak residual stress moved as weld beads were added to the previous weld layers, which can be beneficial in reducing the peak residual stress, particularly in the weld toe area that is a common place of in-service cracking [26]. Research also shows that a flat-laid substrate plate, upon which an AM part is built, contains peak tensile residual stresses on both sides of the weld bead [28]. These stresses correspond to the location of the weld bead toe and are much higher in the longitudinal direction. Although the impact of residual stress on crack growth pattern has been addressed by some researchers [26-28], its effect on the crack growth behavior near the AM-substrate interface has not been investigated.

Experimental investigation on fatigue crack growth behaviour of WAAM Ti-6Al-4V has been conducted by our research group [29-32]. This paper aims at analysing these test results, in particular the crack growth behaviour at the interface between the WAAM alloy and wrought substrate, where the microstructure has changed markedly and residual stress distribution is complex. First, test results of WAAM Ti-6Al-4V

compact tension specimens are studied in terms of the fatigue crack growth rate and trajectory. Second, a finite element model is developed to calculate the residual stress being retained in two different specimens based on the test measurement of a larger WAAM piece, from which the test specimens were extracted. Finally, experimentally measured fatigue crack growth behaviour at the WAAM-wrought interface (in terms of the crack growth rate and trajectory) is illuminated from both the microstructure and residual stress points of view.

2. Experimental

2.1 Manufacturing process and experimental setup

To investigate the fatigue crack propagation behaviour at the interface between WAAM and wrought substrate Ti-6Al-4V alloys, fatigue tests of compact tension (C(T)) specimens were conducted by the same research group [29,31,32]. Fig. 1 shows the specimen layout in a WAAM-substrate "wall" prior to the machining of these specimens. The wall was fabricated by the Welding Engineering and Laser Processing Centre at Cranfield University [32] using an in-house developed system. During the process, metal wire was melted by a plasma torch and the molten metal was deposited on to a substrate or previously deposited layers. As the plasma torch moved along a designed path, the deposited metal formed a layer. After completing a layer, the part was allowed to cool down to below 100^{o}C before a new layer was built. This process was repeated until a complete wall was built. The plasma torch and the substrate are housed in an airtight tent containing argon as the shielding gas. The Liburdi Engineering PW-400C plasma torch was used in this project. Table 1 shows the process parameters that are originally reported in [21, 24, 28].

A total of four walls were manufactured for this project. One of them was used for residual stress measurement, and the other three were used to produce the test specimens as shown in Fig. 1.

Fig. 2 shows the C(T) specimen geometry and dimension that complies with the ASTM standard [33]. This paper investigated two scenarios of crack propagation at the interface between the wrought and WAAM alloys, i.e. Type-A specimen (Fig. 2a) for crack initiating from the substrate and propagating into the WAAM material, and Type-C specimen (Fig. 2b) for crack initiating from the WAAM and propagating into the substrate. When machining these specimens, surface roughness was removed resulting in nominal thickness of 6 mm. Growing crack length during the fatigue test was measured using a travelling microscope. To aid the measurement, scribe lines of 1 mm interval were marked by the Vernier gauge along the potential crack growth path.

Table 1 Process parameters for fabrication of the WAAM-substrate wall [21, 24, 28]

Layers	1-3	4-6	7-9	> 9
Current(A)	160	155	150	145
Arc voltage(V)			20.4	
Wire feed speed (mm/s)			33.3	
Travel speed (mm/s)			4.5	
Plasma gas flow rate (l/min)			0.8	
Torch shielding gas rate (l/min)			8	
Wire diameter (mm)			1.20	
Layer height (mm)			1.25	

Fatigue test was conducted using an Instron Model 8031 servo-hydraulic fatigue testing machine having the maximum load capability of 50 kN. A travelling microscope of X7 magnification factor was used to monitor the crack tip location. To remove the notch root effect, pre-cracking test was conducted until a fatigue crack of 3 mm length was initiated at the notch root. The maximum load for the pre-cracking test was 6 kN with load ratio 0.1 until initiating a 2.5 mm crack. The maximum load was then reduced to 5 kN for a further 0.5

mm crack growth. For the crack growth rate test, the maximum load, load ratio and frequency were 5 kN, 0.1 and 10 Hz, respectively. Three specimens were tested for each configuration.

2.2 Fatigue crack trajectory

Crack growth trajectory was observed on polished specimens in both macroscopic and microscopic scales. On the macroscopic view, crack exhibits a straight extension line for both the type A and C specimens as shown in Fig. 3a and b. This could be explained by both the geometric and applied load symmetry (Fig. 2). However, the optical microscopic observation revealed distinctively different crack growth patterns between the substrate and WAAM. In the substrate, crack propagated in a straight and smooth line (Fig. 4a). At the WAAM-substrate interface, crack extension path changed from straight and smooth to slightly deflected course (Fig. 4b). After passing the interface, crack in the type A specimen entered the WAAM zone and showed a tortuous pattern (Fig. 4c and d). The reason for the different crack growth patterns is discussed in Section 4.

2.3 Fatigue crack growth rate

The incremental polynomial method recommended by ASTM E647 [33] is used to obtain the relationship of fatigue crack growth rate (da/dN) and stress intensity factor range (ΔK). Fig. 5a compares test measured da/dN vs. ΔK curves of the Type A and C specimens. The WAAM-substrate interface location is marked in Fig. 5a where the crack length (a) is 30 mm corresponding to a ΔK value of 23 MPa$\sqrt{\text{m}}$. Type A and C specimens have similar fatigue crack growth rate before the crack reaches the interface. After that, crack propagates faster in Type C than that in Type A.

For comparison, fatigue crack growth rates of two baseline materials (i.e. either wrought or WAAM alloy) are illustrated in Fig. 5b in terms of da/dN vs. ΔK. The wrought alloy data was measured in this study using rolled Ti-6Al-4V from the same material batch as the substrate in the bi-material specimens, same specimen geometry and dimension, and same test machine and load condition. The baseline WAAM alloy curve is taken from [21], which was built by the same Lab. Fig. 5b shows a clear difference in the crack propagation rates in the L-T orientation between the WAAM and wrought alloys. Crack growth rate in the wrought condition is greater than that in the WAAM under the same ΔK.

Figure 6 shows the crack growth rate as a function of the crack length and comparison with that of the two baseline materials (wrought and WAAM only). For the Type A specimen, crack propagates in the substrate first before reaching the WAAM-substrate interface; after the crack has passed the interface, it enters the WAAM alloy. Hence, Fig. 6a compares the crack growth rate with the baseline wrought Ti-6Al-4V prior to crack reaching the interface and then with the baseline WAAM after crack passing the interface. Crack propagates slightly faster than that in the baseline wrought alloy before the interface and then shows similar growth rate with the baseline WAAM after the interface. For the Type C specimen, crack growth rate is compared with the baseline WAAM prior to it reaching the interface since the crack propagates in the WAAM alloy in this stage. Crack growth rate is faster than that in the baseline WAAM. After it crossing the interface, crack enters the substrate and still propagates faster than that of the baseline wrought alloy. It should be pointed out that in the Heat Affected Zone (HAZ, indicated in Fig. 6), mechanical properties (including crack growth rate) could be different from those of the wrought or WAAM alone and crack growth rate in HAZ is difficult to measure. Therefore, fatigue crack growth rate in the HAZ is not discussed in this paper.

2.4 Measurement of residual stress in WAAM-substrate wall

(a) The contour method

Residual stress in the WAAM built wall is measured using the contour method [34], which is particularly attractive as it provides a 2-dimensional (2D) stress map over a cross-section of a component using a single cut. Compared with the diffraction techniques, the contour method is not sensitive to microstructural

variations and has been successfully applied to various weldments [35]. Furthermore, the contour method is not limited by the geometry and thickness of the test components and has been applied to large and complex geometries [36]. It is a destructive method, but in this study we needed to cut the wall anyway to make the C(T) specimens. The main steps of the contour method are: specimen cutting, surface contour measurement, data analysis and finite element analysis (FEA). They are described as follows.

Specimen cutting is the most critical step as all the succeeding steps depend on the quality of the cut faces. Wire electric discharge machining (EDM) best meets the contour method requirements [37]. In this work, an Agie Charmilles wire EDM machine (FI-440CS) with a 150 μm diameter brass wire was used. Prior to contour cutting, the specimens and clamping fixtures were left to reach the thermal equilibrium condition in the EDM deionised water tank.

The normal deformation contours of the opposing cut surfaces were measured using a Zeiss Eclipse coordinate measuring machine (CMM), fitted with a Micro-Epsilon laser probe and a 4 mm diameter ruby-tipped Renishaw PH10M touch trigger probe. The resolution of the Micro-Epsilon laser triangulation displacement sensor is 0.15 μm at the maximum sampling rate and without averaging. The measurement point spacing was on a 0.1 mm grid. The perimeters of the cut parts were further measured with the touch probe to define the geometry of the surfaces for the data processing step.

Noise and outliers are inevitable in the CMM measured raw data. This might be due to the cutting artefacts, surface roughness or random errors in the measurements. Data smoothing was conducted using cubic spline fitting. Several 'knot spacings' (1.5×1.5, 3×3, 5×5 and 7×7 mm^2) were examined. Uncertainty in the calculated stresses at any given node on the cut surface was estimated by taking the standard deviation of the new stress and the previous stress by coarser fit [38]. The minimum average uncertainty in stress was 6 MPa corresponding to an optimum knot spacing of 3×3 mm^2 in this case.

3D finite element models based on the measured perimeter of the cut parts were built using the ABAQUS code [39]. Linear hexahedral elements with reduced integration (C3D8R) were used in the models. The test piece was assumed to have homogeneous and isotropic elastic properties with a Young's modulus of 113.8 GPa and Poisson's ratio of 0.342 since the difference in Young's modulus in the two major directions of WAAM alloy is small [21]. Smoothed displacement data were evaluated and applied as the boundary conditions, with reverse sign, at the cut surface nodes of the FE models. Linear elastic stress analyses were performed to calculate the residual stresses normal to the cut faces.

(b) Measurement result

A 2D contour map of the longitudinal stress measured by the contour method is shown in Fig. 7(a). Moving from the top of the wall towards the interface, the stresses in the WAAM layers are tensile near the top and gradually decrease and turn into compression with the highest stress of the order of ±150 MPa. The higher stresses were measured in the substrate with the maximum tensile stress (430 MPa) near the bottom and a large region of high compressive stress accumulated below the interface. To present this stress field more clearly, a 1D stress distribution is shown in Fig. 7b, representing the stress along the mid-thickness line.

Both Figs. 7a and b show significant residual stress in the longitudinal direction (i.e. the welding torch movement direction). An analytical method of residual stress generation in an AM piece is described in [40]. The principle should be applicable to AM panels of different size, material and process methods. Residual stress is developed and accumulated layer by layer due to the combined action of material shrinkage and bending, resulting in tensile residual stress on the top part of the AM wall and bottom part of the substrate. To satisfy the equilibrium condition, compressive residual stress exits in the region around the interface of substrate and AM. Measured residual stresses in the wall agree very well with the stress distribution example by analytical calculation in [40].

3. FE analysis of residual stress in C(T) specimens and resultant stress intensity factor

Based on the measured residual stress in the WAAM-substrate wall, finite element analysis (FEA) was conducted to calculate the residual stress being retained in the C(T) specimens and the resultant crack tip stress intensity factors.

3.1 FE model

To evaluate the residual stress retained in the C(T) specimens, a finite element (FE) model is developed to simulate the cutting of C(T) specimen from the WAAM wall. Fig. 8a shows the wall model using the plane-strain elements (second order isoperimetric element designated as CPE8 in ABAQUS. Total number of element is 59050). At the crack tip (Fig. 8c), the singularity mesh method [39], i.e. moving the middle nodes on the sides connected to the crack tip to the quarter point nearest to the crack tip, is adopted to model the crack tip stress singularity of the order of $r^{-1/2}$, where r is the distance from the crack tip. The minimum size of elements around the crack tip is 0.007 mm, which is smaller than the radius of the theoretical plastic zone. Residual stress induced stress intensity factor (K_{res}) is calculated by the FE model to study its effect on crack propagation.

The cutting process can be regarded as a simple stress relief process due to the material removal [41]. Element removal model [39] is available in ABAQUS that can be used to remove a part of the model to simulate the machining process. Fig. 9 illustrates the five steps of element removal procedure to simulate the process of cutting the C(T) specimen. (1) Prior to the removal step, measured residual stress (Section 3.1) is inputted into the FE model as an initial stress condition (Fig. 9a) using a user defined subroutine (SIGINI). (2) Apply equilibrium condition to the initial residual stress in the whole wall (Fig. 9b), and check residual stress distribution to ensure an equilibrium stress state is established at the end of this step. (3) Remove the elements around the specimen "block" and inside the perimeter of the loading holes (Fig. 9c). (4) Eliminate some elements to create the notch (Fig. 9d). (5) Release the boundary condition on the crack line to obtain the crack tip stress distribution and stress intensity factor (K_{res}) as the result of the retained residual stress in the C(T), Fig. 9e. It should be pointed out that in each modelling step only the appropriate and necessary boundary conditions are introduced (Fig. 9) to constrain the rigid body displacement.

3.2 FE results and discussion

Fig. 10 shows the residual stress distribution in a material block of the size of the C(T) specimen with the holes but without the notch (after the Step 3 of the element removal procedure), representing the original residual stress state in the test specimen after being extracted from the wall but without the notch and crack. For the Type A specimen (crack grows from substrate to WAAM), residual stress is released significantly owing to the creation of the holes (comparing Fig. 10a and 10c) as the compressive residual stress being removed is relatively high. However, for the Type C specimen (crack grows from WAAM to substrate), the hole cutting only slightly affects the residual stress redistribution (Fig. 10b and 10d) as the holes are in a region of relatively low stress. For clarity, stress distribution along the specimen centre line is shown in Fig. 10e and 10f.

Figure 11 presents calculated residual stress intensity factors (K_{res}) versus the crack length. To demonstrate the degree of stress concentration as the residual stress evolve with the growing crack, a series of stress contour maps near the crack tip of various crack lengths are inserted for the two configurations. The extent of stress concentration can be estimated by the size of stress concentration area as well as the stress intensity factor. Following observations can be made.

(1) Type A specimen (Fig. 11, insert a, b and c): there is a concentrated compressive stress area near the crack tip at the crack length of 20 mm (Fig. 11a). After that, residual stress turns to tensile and causes stress concentration near the crack tip. The resultant stress intensity factor (K_{res}) reaches its peak value of 1.51 MPa$\sqrt{m}$ at a = 30 mm (Fig. 11b). There is almost no stress concentration (K_{res}= -0.08 MPa$\sqrt{m}$) at a = 50 mm (Fig. 11c). This can be explained by Fig. 10e showing residual stress distribution along the crack

propagation line. There is an area of significant compressive stress in the region of $-7 < X < 27$ mm (X is the distance from the loading hole centre point line), which results in the crack tip being subjected to compressive residual stress at a = 20 mm. During the crack extension, the release of the compressive residual stresses results in the increase of K_{res}, which has the peak value at a = 30 mm. Most residual stresses are released after the crack has propagated out of the compressive stress area; consequently much lower K_{res}.

(2) Type C specimen (Fig. 11, insert d, e and f): crack tip is in tensile residual stress zone in the crack length range of 20 to 50 mm. Residual stress induced stress intensity factor K_{res} increases with the crack length and at a = 36 mm it reaches the peak value of 12.2 $MPa\sqrt{m}$ (Fig. 11e). This could also be reasonably explained by Fig. 10f showing the residual stress in the centre line of the specimen. High compressive residual stress zone locates at $34<X<58$ mm, resulting in high tensile stress concentration near the crack tip due to the equilibrium of the stress field. When crack enters the compressive residual stress zone, residual stress releases at a >34 mm. Therefore, residual stress intensity factor decreases with the crack propagation.

(3) Residual stress causes greater stress concentration near the crack tip and higher K_{res} for the same crack length in Type C specimen than that in Type A. This difference can be explained by the following two aspects. (a) The loading hole location. For Type A, removal of the hole material releases residual stresses significantly, since they are in the high compressive residual stress area. However, for Type C, the drilling loading holes only slightly decreases the residual stress, since residual stress in the hole area is low. (b) The notch and crack location. For Type A, crack grows from substrate to WAAM, i.e. crack enters the high compressive residual stress area immediately after its initiation. Both notch cutting and crack growth release residual stresses significantly. In contrast, crack grows from WAAM to substrate in Type C specimen, residual stress is reduced a little as the notch cutting and crack location is far away from the high compressive residual stress zone.

4. Results and discussion

4.1 Influence of microstructure

As mentioned in Section 2, crack manifests different trajectory and growth rates in the substrate and WAAM alloys. The microstructure characteristics of substrate (wrought) and WAAM Ti-6Al-4V are shown in Fig. 12.

The optical microstructure of substrate Ti-6Al-4V is demonstrated in Fig. 12a. It could be described as a type of α+β equiaxed structure, which is the same as most high strength Ti-6Al-4V used in the airframes. Primary α grains account for approximately 70% and the others are occupied by lamellar α and β colony. In addition, the grain size of the substrate material is quite fine, and the diameter of the globular primary α grains is less than 10 micron. For comparison, the optical microstructure of WAAM produced Ti-6Al-4V is demonstrated in Fig. 12b. The lamellar structure with an average α lamellae lath width of about 1 micron can be seen. No complete columnar β grain could be obtained, since its width is about 2 mm that could not be seen in this magnification. The microstructure of WAAM Ti-6Al-4V could be characterized as the Widmanstätten lamellar structure that is also reported for WAAM [15] and other AM process produced titanium alloys [18,19]. The Widmanstätten lamellar is similar to that of the extra low interstitial (ELI) Ti-6Al-4V as shown in Fig. 12c [42]. The lamellar structure has especially high fracture toughness and excellent damage tolerant properties [9,42-44]. This could explain why the WAAM Ti-6Al-4V has slower crack growth rate than that of the wrought condition substrate (Fig. 5b).

The different crack growth trajectories between the substrate and WAAM Ti-6Al-4V may also be attributed to the microstructure difference. In the substrate, crack propagates smoothly (Fig. 4a) in the fine α+β equiaxed structure as in the wrought Ti-6Al-4V. In the WAAM, crack takes a tortuous route (Fig. 4c and d) owing to the lamellar structure (Fig. 12d). The tortuous crack path is shown to increase the resistance to fatigue crack propagation [18].

4.2 Influence of residual stress

FE work presented in Section 3 indicates that residual stresses in the C(T) specimens cause stress concentration near the crack tip; consequently they affect the crack growth rate. Effect of residual stress on the maximum stress intensity factor (K_{max}) are shown Fig. 13, where $K_{tot,\,max}=K_{app,\,max}+K_{res}$, and $K_{app,\,max}$ is the maximum stress intensity factor corresponding to the maximum applied load of 5 kN. It can be seen from Fig. 13 that $K_{tot,\,max}$ varies with the residual stress distribution for both types of the specimens, i.e. residual stress can also affect the crack growth rate as shown in Fig. 6a and b. It should be pointed out that the effect of residual stress on $K_{tot,\,max}$ in Type A is much smaller than that in Type C specimen. This can be explained by the FE models in Section 3.2. For the Type A specimen, residual stress is released significantly with the notch cutting and crack extension; hence it has little effect on the $K_{tot,\,max}$ (Fig. 13) and fatigue crack growth rate. For the Type C specimen, however, residual stress significantly enhances the $K_{tot,\,max}$ (Fig. 13) as it causes higher stress concentration near the crack tip and greater K_{res}, resulting in greater crack growth rate than that in the substrate material.

In summary, both microstructure and residual stress affect the fatigue crack growth behaviour of WAAM specimens when crack is perpendicular to the wrought-WAAM interface. The authors would also like to understand how the microstructure and residual stress affect crack growth pattern when crack is parallel to the interface, which is on-going.

5. Conclusions

Microstructure and residual stress are investigated in order to understand their effects on fatigue crack propagation behaviour in specimens containing an interface between wrought substrate and WAAM Ti-6Al-4V. Based on the analyses, following conclusions can be drawn.

(1) The difference in crack growth rate and pattern in the substrate and WAAM is attributed to the different microstructure characteristics. Crack propagates in straight and smooth line in the wrought condition that has equiaxed structure, but in tortuous path in the WAAM alloy owing to the lamellar structure. Consequently, WAAM alloy has lower crack propagation rate than the substrate.

(2) There are considerable residual stresses in the wall of WAAM alloy built upon a wrought substrate. Retained residual stress in the C(T) specimens affects the crack growth rate when it is near the interface between WAAM and substrate. The magnitude of residual stress effect depends on the crack location and propagation direction. When crack propagates from substrate to WAAM (Type A specimen), residual stress is released immediately due to the cutting of the holes and the notch; thus it has little effect on subsequent crack propagation. In contrast, if crack propagates from WAAM to substrate (Type C specimen), residual stress causes considerable increase in the total stress intensity factor; consequently greater crack propagation rate.

Acknowledgement: The authors gratefully acknowledge the China Scholarship Council and the Aviation Industry Corporation of China for financial support, Cranfield University Welding and Laser Processing Centre for producing test specimens, Nicholas Hills and Dongni Wang for conducting part of the test and characterization.

References

[1] C.H. Che-Haron, A. Jawaid, The effect of machining on surface integrity of titanium alloy Ti-6Al-4V, J. Mater. Process. Technol. 166 (2005) 188-92

[2] E.O. Ezugwu, Z.M. Wang. Titanium alloys and their machinability - a review. J. Mater. Process. Technol. 68 (1997) 262-274

[3] A.A. Antonysamy, J. Meyer, P.B. Prangnell, Effect of build geometry on the β-grain structure and texture in additive manufacture of Ti-6Al-4V by selective electron beam melting. Mater. Charact. 84 (2013) 153-168

[4] W.E. Frazier, Metal Additive Manufacturing: A Review, J. Mater. Eng. Perform. 23 (2014) 1917-1928

[5] F. Martina, J. Mehnen, S.W. Williams, et al, Investigation of the benefits of plasma deposition for the additive layer manufacture of Ti-6Al-4V, J. Mater. Process. Technol. 212 (2012) 1377-1386

[6] F. Wang, S.W. Williams, M. Rush. Morphology investigation on direct current pulsed gas tungsten arc welded additive layer manufactured Ti6Al4V alloy, Int. J. Adv. Manuf. Tech. 57 (2011) 597-603

[7] E. Brandl, B. Baufeld, C Leyens, et al, Additive manufactured Ti-6AL-4V using welding wire: comparison of laser and arc beam deposition and evaluation with respect to aerospace material specifications, Phys. Procedia. 5 (2010) 595-606

[8] P.A. Colegrove, H.E. Coules, J. Fairman, et al. Microstructure and residual stress improvement in wire and arc additively manufactured parts through high-pressure rolling. J. Mater. Process. Technol. 213 (2013) 1782-1791

[9] G. Lutjering Influence of processing on microstructure and mechanical properties of (α+β) titanium alloys, Mater. Sci. Eng., A 243 (1998) 32-45

[10] B. Baufeld, O. Van der Biest, Mechanical properties of Ti-6Al-4V specimens produced by shaped metal deposition, Sci. Technol. Adv. Mater. 10 (2009) 1-10

[11] B. Baufeld, E. Brandl, O Van der Biest, Wire based additive layer manufacturing: comparison of microstructure and mechanical properties of Ti-6Al-4V components fabricated by laser-beam deposition and shaped metal deposition. J. Mater. Process. Technol. 211 (2011) 1146-1158

[12] S.M. Kelly, S.L. Kampe, Microstructural evolution in laser-deposited multilayer Ti-6Al-4V builds: part I. microstructural characterization, Metall. Mater. Trans. A 35 (2004) 1861-1867

[13] S.M. Kelly, S.L. Kampe, Microstructural evolution in laser-deposited multilayer Ti-6Al-4V builds: part II. thermal modeling. Metall. Mater. Trans. A 35 (2004) 1869-1879

[14] K. Taminger, R. Hafley, Electron beam freeform fabrication for cost effective near-net shape manufacturing. NATO/RTOAVT-139 Specialists' Meeting on Cost Effective Manufacture via Net Shape Processing, Amsterdam, the Netherlands, 2006: 9-25

[15] F. Wang, S.W. Williams, P. Colegrove, et al, Microstructure and mechanical properties of wire and arc additive manufactured Ti-6Al-4V, Metall. Mater. Trans. A 44 (2013) 968-977

[16] E. Brandl, F. Palm, V. Michailov, et al, Mechanical properties of additive manufactured titanium (Ti-6Al-4V) blocks deposited by a solid-state laser and wire, Mater. Des. 32 (2011) 4665-4675.

[17] B. Baufeld, O. Van der Biest, R. Gault, Additive manufacturing of Ti-6Al-4V components by shaped metal deposition: microstructure and mechanical properties, Mater. Des. 31(2010) S106-S111

[18] G. Schroeder, J. Albrecht, G. Luetjering. Fatigue crack propagation in titanium alloys with lamellar and bi-lamellar microstructures. Mater. Sci. Eng., A 319-321 (2001) 602-606.

[19] A.A. Antonysamy, Microstructure, texture and mechanical property evolution during additive manufacturing of Ti6Al4V alloy for aerospace applications, PhD Thesis, 2012, University of Manchester

[20] S. Liu, The effect of oxygen content on the fracture toughness of additively manufactured Ti-6Al-4V, MSc Thesis, 2015, Cranfield University.

[21] E. Lorant, Effect of microstructure on mechanical properties of Ti-6Al-4V structures made by additive layer manufacturing. MSc Thesis, 2010, Cranfield University

[22] P. Edwards, A. O'Conner, M. Ramulu, Electron beam additive manufacturing of titanium components: properties & performance, J. Manuf. Sci. E-T ASME, 135 (2013): 061016/1-7

[23] P. Edwards, M. Ramulu, Effect of build direction on the fracture toughness and fatigue crack growth in selective laser melted Ti-6Al-4V, Fatigue Fract. Engng. Mater. Struct., 38 (2015): 1228- 1236.

[24] J. Ding, P. Colegrove, J. Mehnen, et al, Thermo-mechanical analysis of wire and arc additive layer manufacturing process on large multi-layer parts. Comput. Mater. Sci. 50 (2011) 3315-3322

[25] P. Rangaswamy, T.M. Holden, R.B. Rogge, et al. Residual stresses in components formed by the laser-engineered net shaping (LENS®) process, J. Strain Anal. Eng. Des. 38 (2003) 519-527

[26] A. Paradowska, J.W.H. Price, R. Ibrahim, et al, A neutron diffraction study of residual stress due to welding, J. Mater. Process. Technol. 164-165 (2005): 1099-1105

[27] T.R. Gurney, Fatigue of welded structures, Cambridge University Press, London. 1968

[28] P.M.S. Almeida, Process control and development in wire and arc additive manufacturing. PhD Thesis, 2012, Cranfield University,

[29] N. Hills, Fatigue crack propagation behaviour at the interface of additively manufactured Ti-6Al-4V and the substrate. MSc Thesis, 2014, Cranfield University

[30] D. Wang, Characterisation of microstructure and fatigue crack behaviour of wire and arc additively manufactured Ti-6Al-4V. MSc Thesis, 2015, Cranfield University

[31] Zhang X. Fatigue & fracture behaviour of additively manufactured Ti-6Al-4V, Presented at WAAMMat Industrial Day, Bedford, UK, March 31, 2015 (unpublished).

[32] A. Addison, J. Ding, F. Martina, H. Lockett, S.W. Williams, X. Zhang, Manufacture of complex titanium parts using Wire+Arc Additive Manufacture, Titanium Europe 2015 - International Titanium Association, 11-13 May 2015, Birmingham, UK

[33] ASTM E647-13. Standard Method for measurement of fatigue crack growth rates, American Society for the Testing of Materials, 2013

[34] M.B. Prime, M.R. Hill, A.T. DeWald, et al, Residual stress mapping in welds using the contour method, Proceedings of the 6th international conference: trends in welding research, 2002,891– 896.

[35] F. Hosseinzadeh, M.B Toparli, P.J Bouchard, Slitting and contour method residual stress measurements in an edge welded beam, J. Press. Vessel Technol., 134(2011), 011402-1-6

[36] M.B. Prime, Contour method advanced applications: hoop stresses in cylinders and discontinuities," in Proc. of the Soc. for Exp. Mechanics Series, 836(2011), 13–28.

[37] W. Cheng, I. Finnie, M. Gremaud, et al, Measurement of near surface residual stresses using electric discharge wire machining. J. Eng. Mater. Technol., 116(1994),

[38] M.B. Prime, R.J. Sebring, J.M. Edwards, et al. Laser surface-contouring and spline data- smoothing for residual stress measurement, Exp. Mech., 44(2004),176–184

[39] ABAQUS 6.13, ABAQUS/Standard Documentation Version 6.13.2, 2013

[40] M. Shiomi, K. Osakada, K. Nakamura, et al, Residual stress within metallic model made by selective laser melting process, CIRP Annals - Manufacturing Technology, 53 (2004) 195-98.

[41] V. Dattoma, M. De Giorgi, R. Nobile, On the evolution of welding residual stress after milling and cutting machining. Comput. Struct. 84 (2006) 1965-1976

[42] Ti-6Al-4V ELI Titanium Alloy. http://www.arcam.com/, accessed May 2015

[43] S. Li, B. Xiong, S. Hui, Effects of cooling rate on the fracture properties of TA15 ELI alloy plates. Rare Metals. 26 (2007) 33-38

[44] J. Zhang, X. Cheng, Z. Li, Total fatigue life prediction for Ti-alloys airframe structure based on durability and damage-tolerant design concept. Mater. Des. 31 (2010) 4329-42

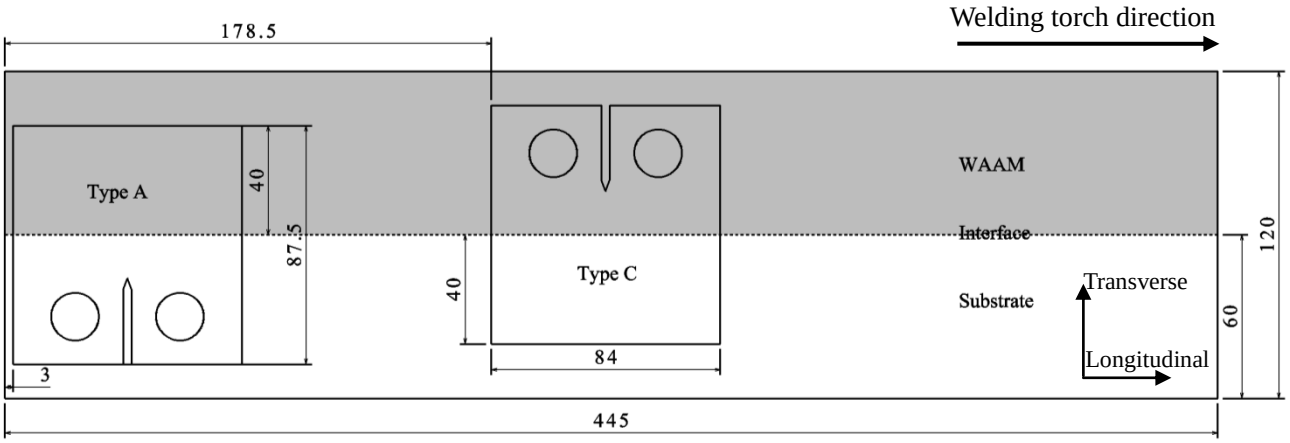

Fig. 1 Layout of two types of test specimen on a WAAM-substrate wall (unit: mm)

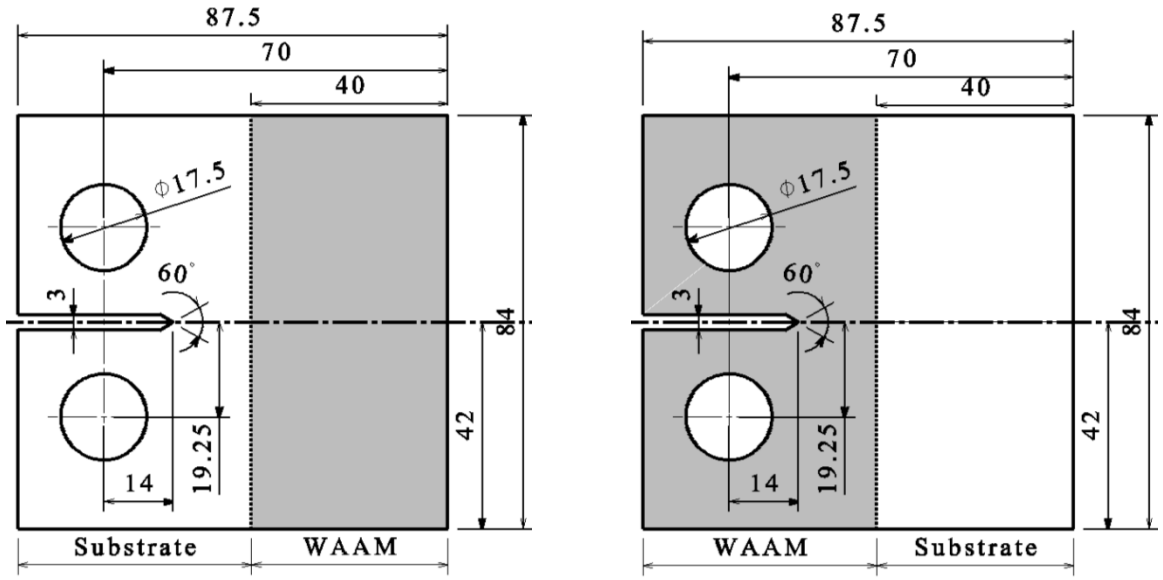

(a) Type A (b) Type C

Fig. 2 Geometry and dimension of C(T) specimens (unit: mm; thickness = 6 mm)

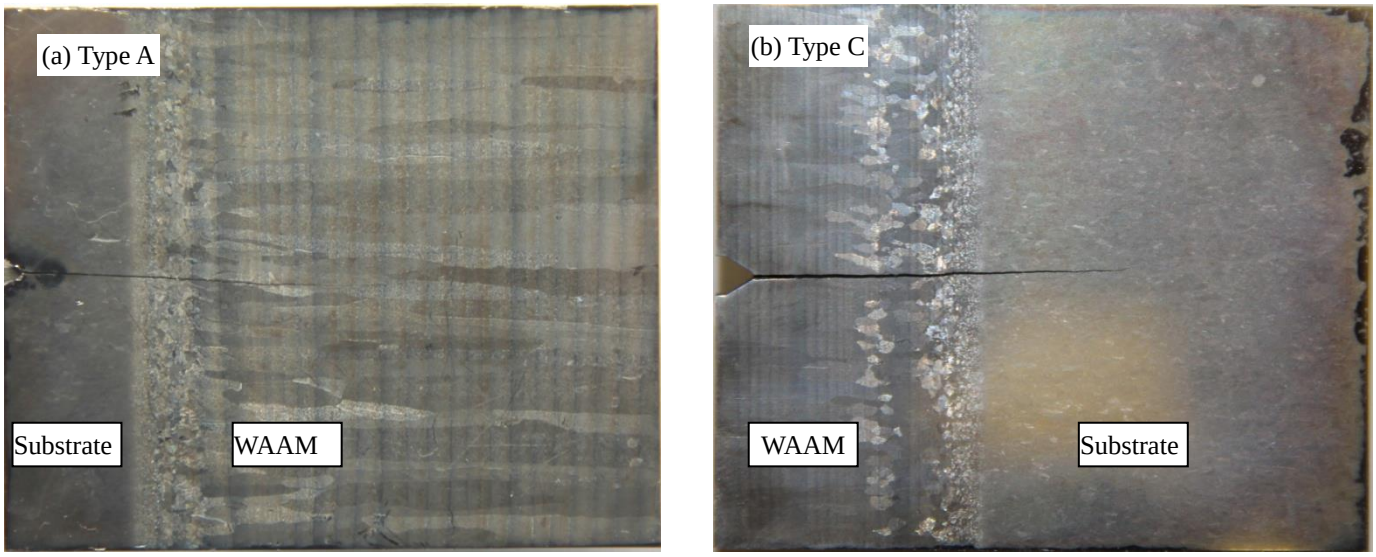

Fig.3 Macroscopic photographs showing fatigue crack propagation trajectory

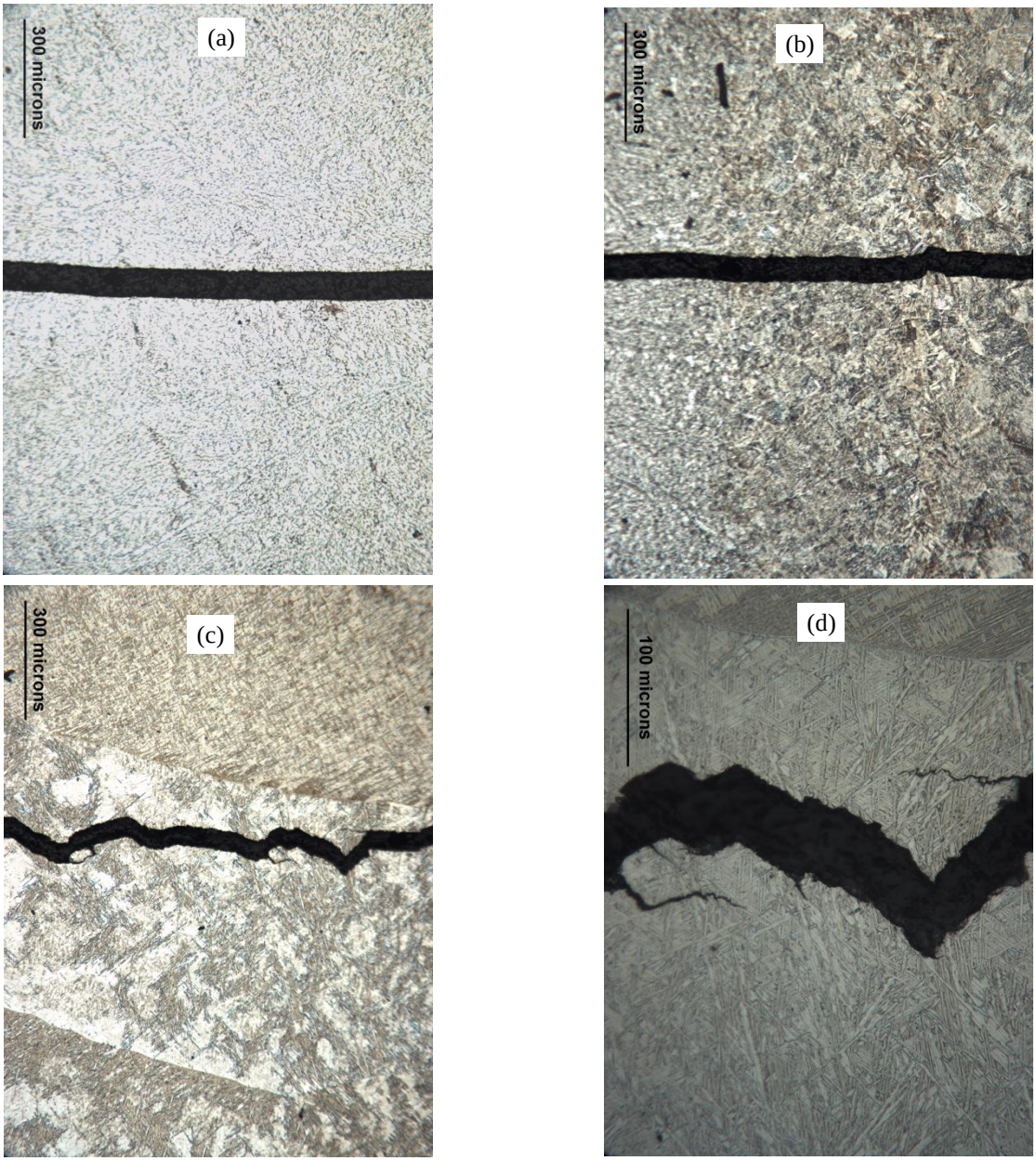

Fig. 4 Optical micrographs of crack growth pattern in the substrate (a), WAAM-substrate interface (b), and WAAM region (c and d) (Type-A specimen)

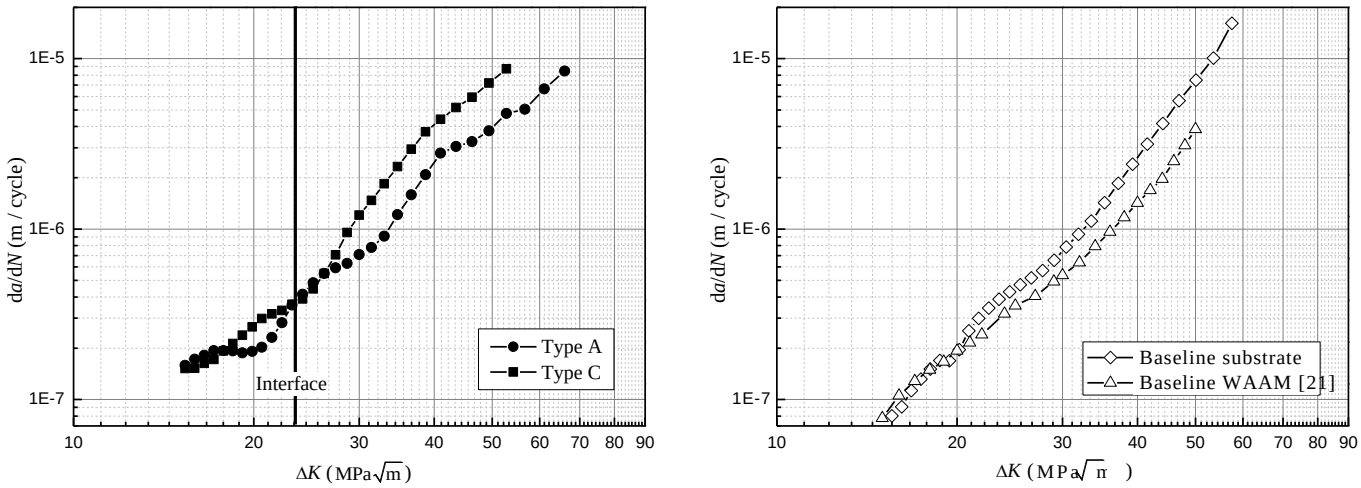

Fig. 5 Comparison of fatigue crack propagation rate (d*a*/d*N*) versus stress intensity factor range (Δ*K*): (a) Type A and C specimens, (b) baseline wrought and WAAM alone Ti-6Al-4V

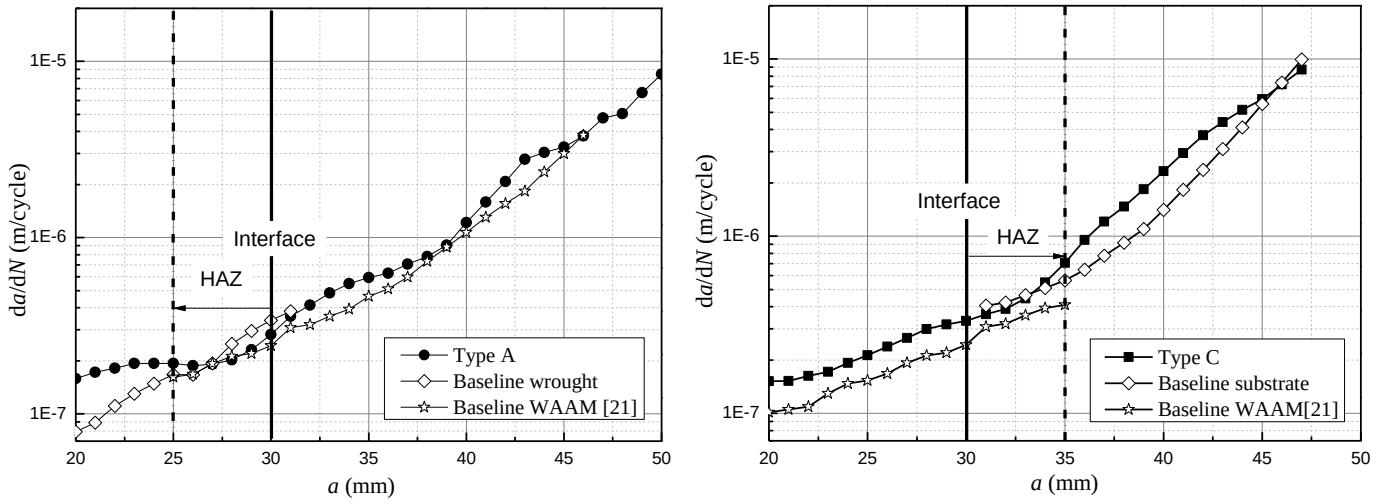

Fig. 6 Comparison of fatigue crack propagation rate (d*a*/d*N*) versus crack length (*a*): (a) Type A: baseline wrought and WAAM alone, (b) Type C: baseline wrought and WAAM alone

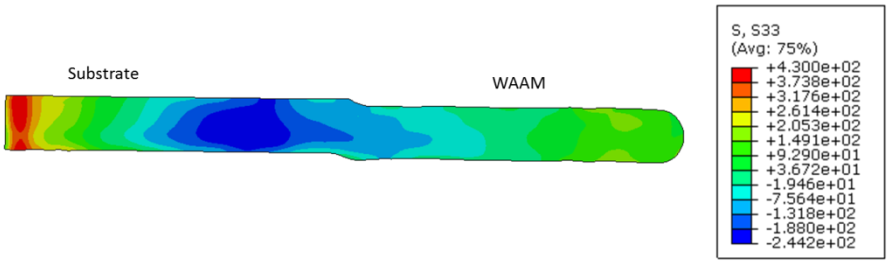

(a) 2D stress map

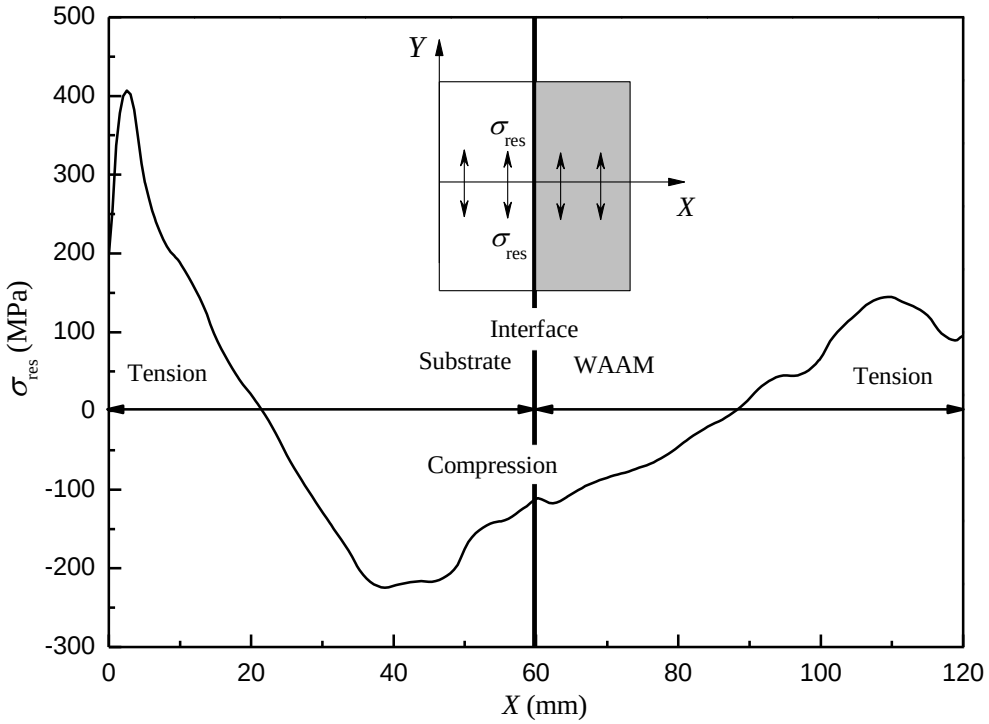

(b) 1D stress distribution along the mid-thickness line

Fig. 7 Residual stress distribution in the WAAM-substrate wall measured by the contour method

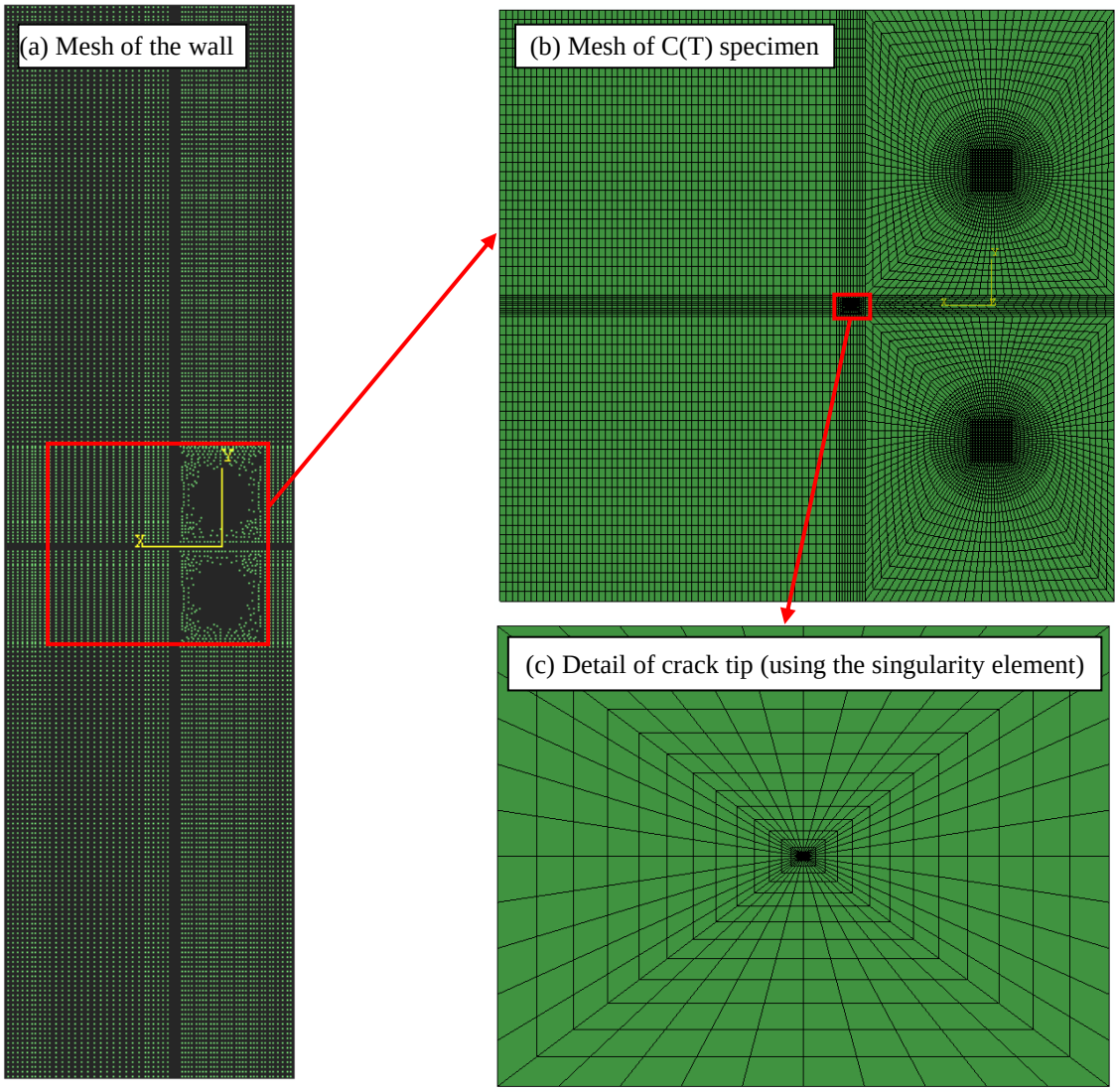

Fig. 8 Finite element model for calculating residual stress in C(T) specimen

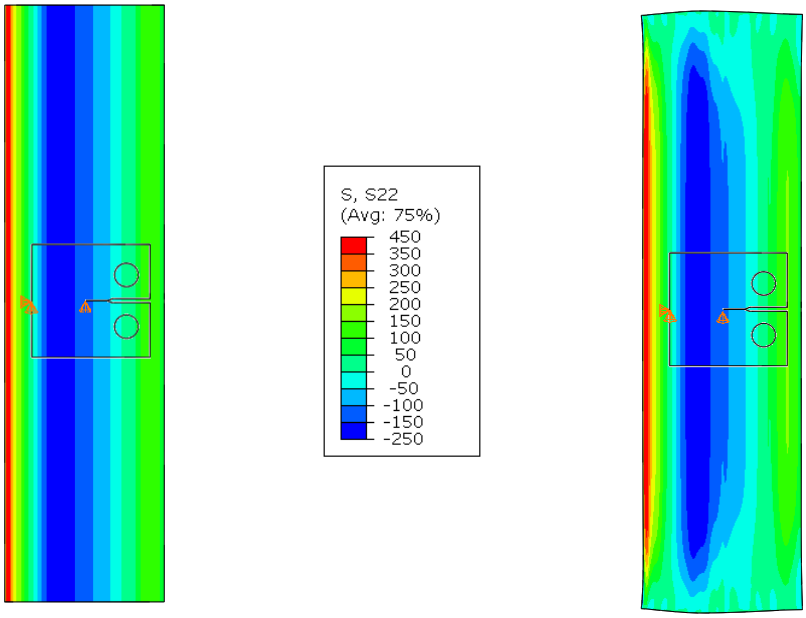

(a) Residual stress input in WAAM-substrate wall (b) Stress equilibrium step

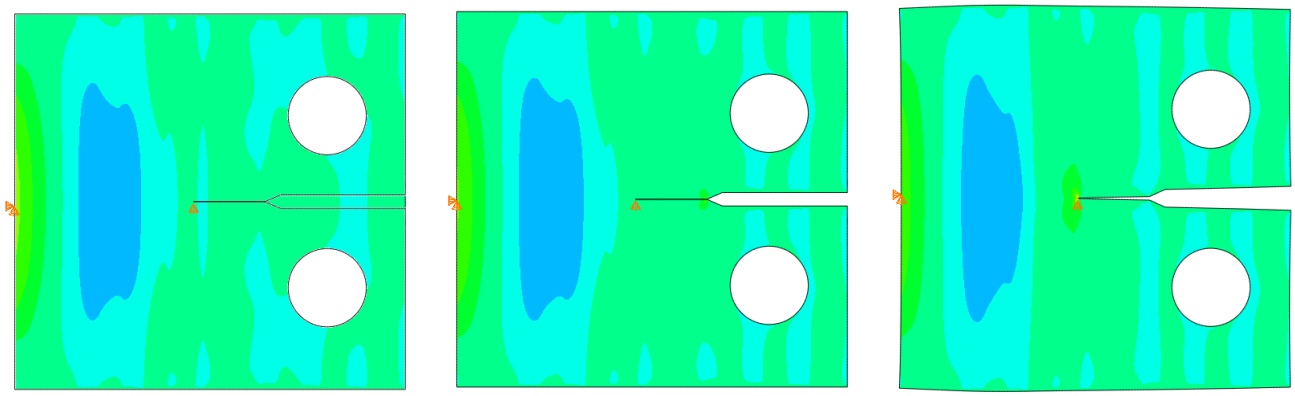

(c) Block and hole cutting (d) Notch cutting (e) Crack release

Fig. 9 Procedure of residual stress calculation in the C(T) specimen (Type C, a = 30mm, unit: MPa)

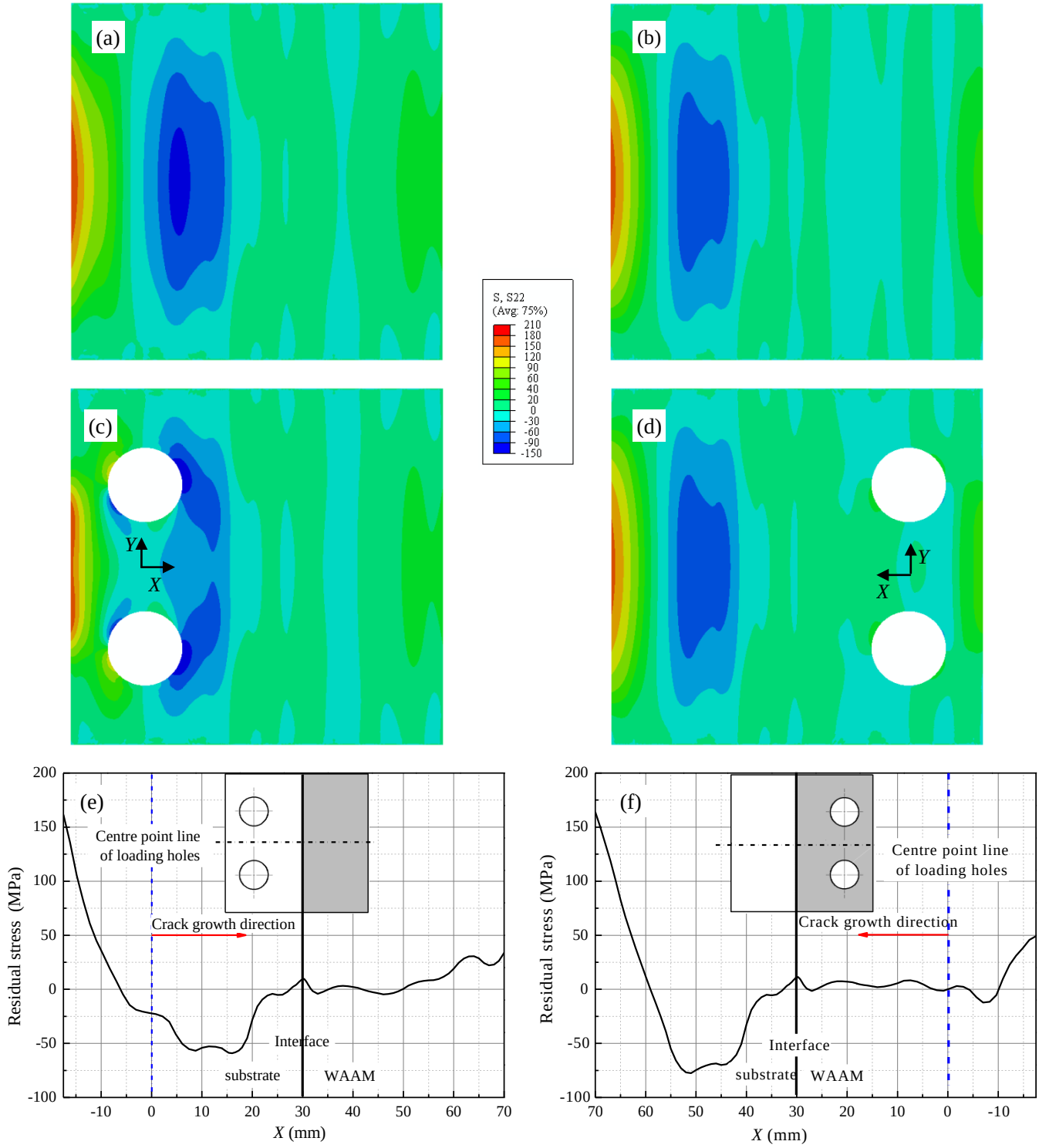

Fig. 10 Residual stress distribution in the C(T) specimen, stress contour of: block of Type A (a) and Type C (b), after hole drilling of Type A (c) and Type C (d), and residual stress along the centre line (Y=0) for: Type A (e) and Type C (f) specimen after hole drilling (unit: MPa)

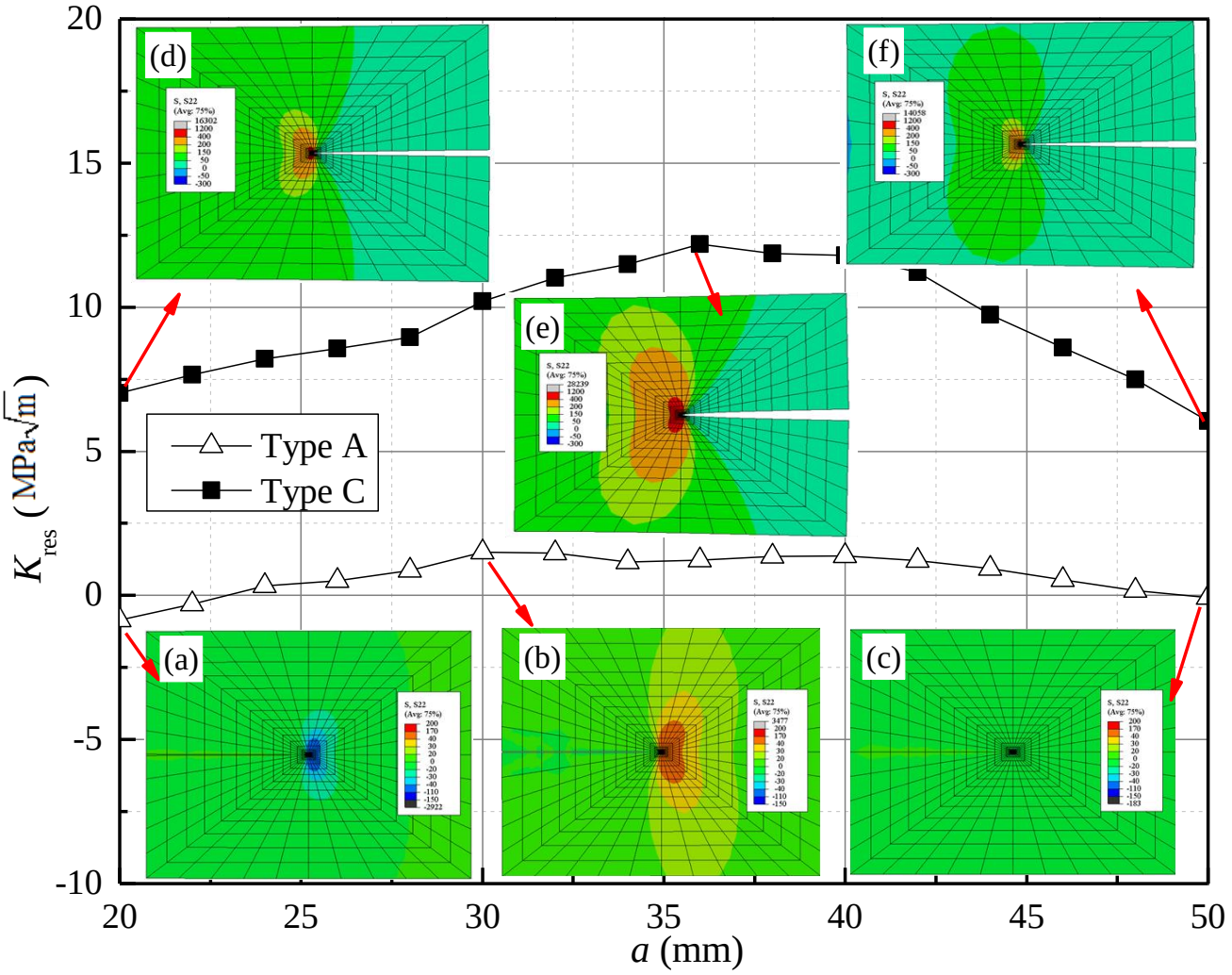

Fig. 11 Distribution of residual stress intensity factor (K_{res}) versus crack length; inserted contour maps showing stress distribution near the crack tip at several crack lengths (unit: MPa)

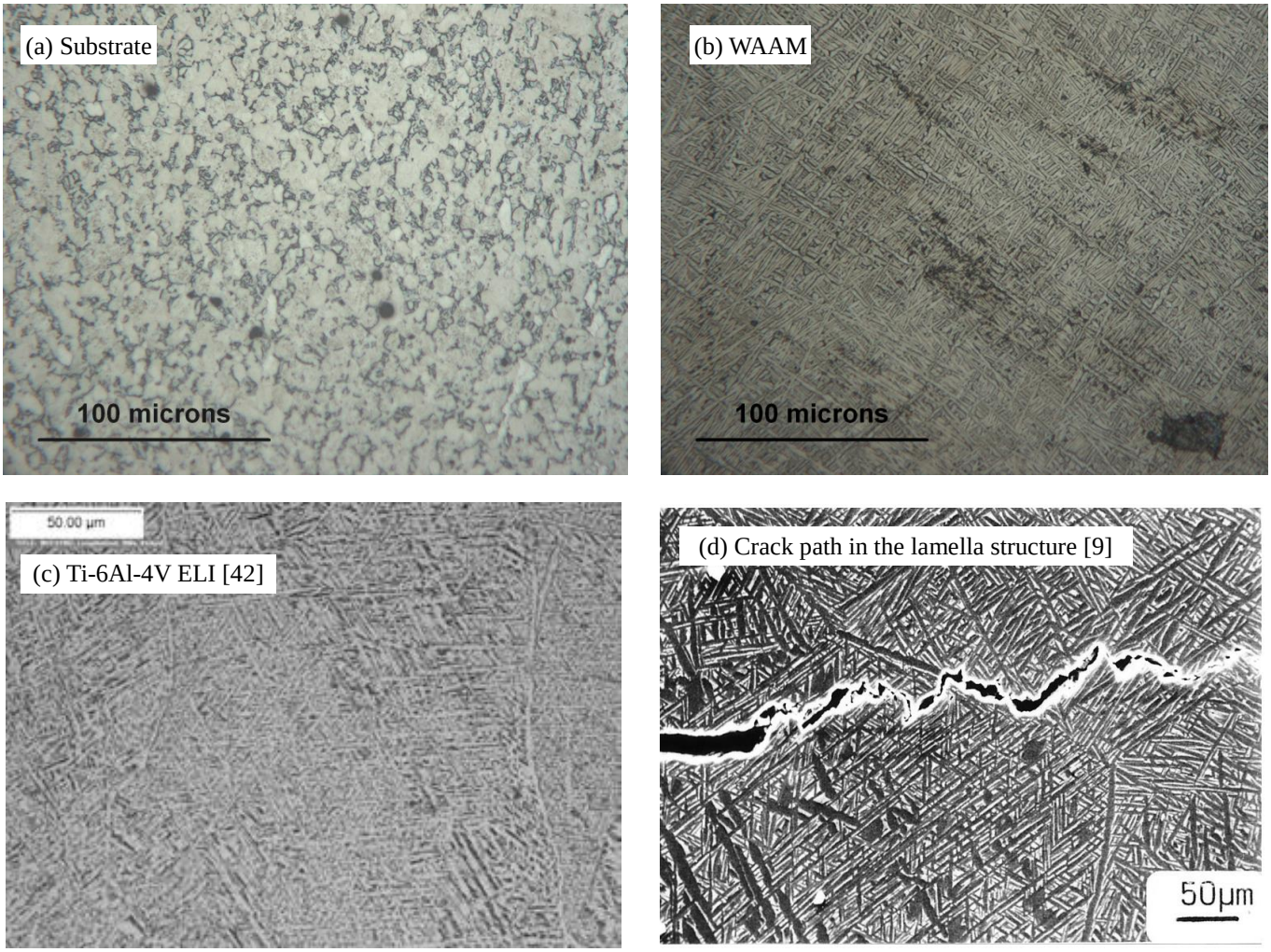

Fig. 12 Microstructure and crack path of various Ti-6Al-4V alloys

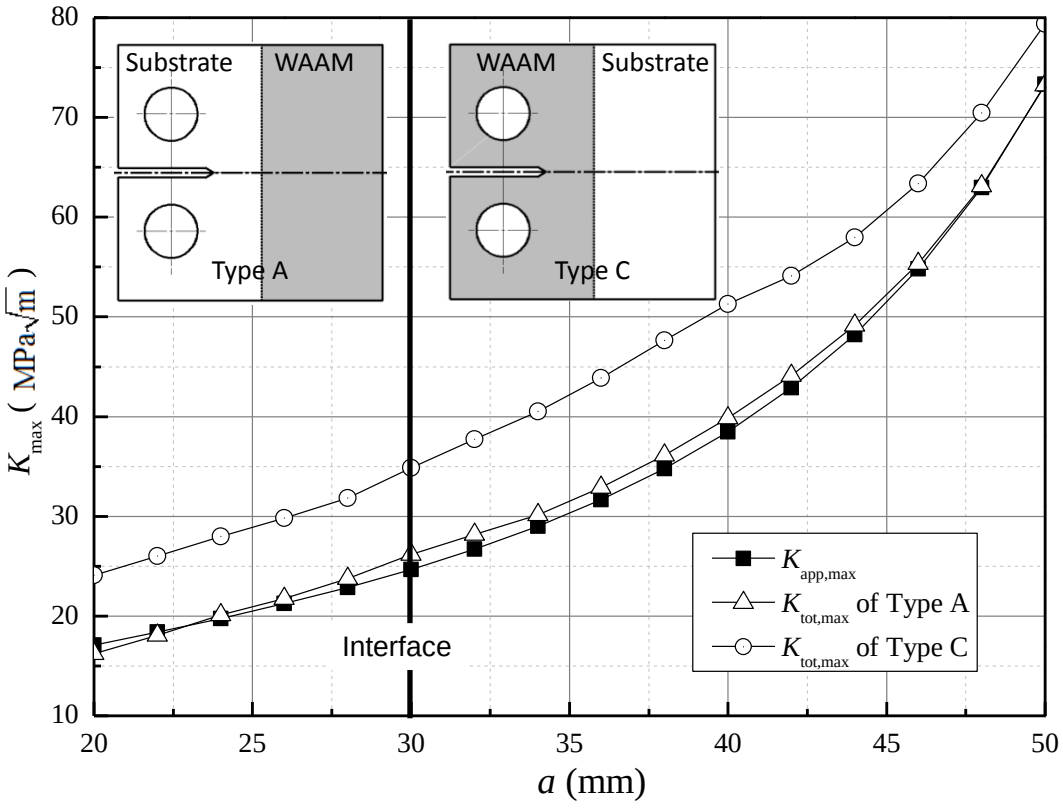

Fig. 13 Residual stress effect on the maximum stress intensity factor ($K_{tot,\,max}$= $K_{app,\,max}$ + K_{res})